Journal of Materials Chemistry C

Materials for optical, magnetic and electronic devices

rsc.li/materials-c

ROYAL SOCIETY
OF CHEMISTRY

PAPER
Ki-Jeong Kim, Bongjin Simon Mun *et al.*
Nature of the surface space charge layer on undoped
SrTiO₃ (001)

Journal of Materials Chemistry C

Nature of the surface space charge layer on undoped SrTiO₃ (001)†

Hojoon Lim, [ID] ‡[a] Chanyang Song,‡[a] Minsik Seo, [ID] [a] Dongwoo Kim,[a] Moonjung Jung, [ID] [a] Habin Kang,[a] Seunghwan Kim,[a] Kyung-Jae Lee,[a] Youngseok Yu, [ID] [b] Geonhwa Kim,[c] Ki-Jeong Kim*[c] and Bongjin Simon Mun [ID] *[ad]

SrTiO₃, an ABO₃-type perovskite structure, has been a popular choice of substrate for many important heterostructures, *e.g.*, ferroelectric thin films and superlattices. As numerous exotic physical phenomena are closely related to delicate electron/ion exchanges at the interfacial layer between the substrate and overlayer, precise characterization of surface/interfacial properties has become the center of many research studies. In most cases of SrTiO₃ research, Nb-doping is applied on the SrTiO₃ surface in order to characterize electrical properties with a negligible effect of contact potential between SrTiO₃ and overlayer. On the other hand, the presence of doping can possibly interfere with a correct interpretation of the surface defect states, which become critical to apprehend the electrical properties of heterostructures. In this report, the undoped SrTiO₃ (001) surface is investigated utilizing ambient-pressure XPS (AP-XPS) and low energy electron diffraction (LEED). We identified the complete chemical/structural/electronic states of O and Sr vacancies on the undoped SrTiO₃ surface from ultra-high vacuum (UHV, $<10^{-9}$ mbar) to O₂ gas pressure of 0.1 mbar conditions. Under oxygen pressure conditions, chemically stable SrO₁₊ₓ surface oxide with a c(6 × 2) superstructure is formed, generating electron depletion and band bending, *i.e.*, the formation of a space charge layer underneath the surface. On the other hand, under UHV, the surface oxide comes from the O vacancy, which has different electronic properties from those of Sr vacancy-related oxides.

1. Introduction

Complex oxide heterostructures with an ABO₃-type perovskite structure have shown remarkable physical phenomena, which include colossal magnetoresistance (CMR), metal–insulator transition (MIT), high T_c superconductivity, and two-dimensional electron gas (2DEG).[1–7] Although the interfacial layers where different complex oxides form are mainly responsible for these exotic features, the exact functionality or working mechanism of oxides at the interface layer is yet fully understood.[1–3,8–11] Having ABO₃-type perovskite structures, SrTiO₃ has suitable lattice mismatch for many overlayer oxides

with ideal chemical/thermal stability from centrosymmetric cubic structures and has been a popular choice for many important heterostructures,[12–15] *e.g.*, LaTiO₃/SrTiO₃ for quasi-two-dimensional electron gas systems, ZrO₂:Y₂O₃/SrTiO₃ for colossal ionic conductivity oxides, and CaCuO₂/SrTiO₃ for high temperature superconductors.[7,16,17] From the results of many previous research studies on heterostructures with SrTiO₃, most of the interfacial properties such as inter-diffusion, symmetry breaking, charge rearrangement, and interfacial strain, are known to have critical effects on the physical/chemical, mechanical, and electrical properties of the system.[1–3,7,16,18] Consequently, the preparation and control of the interfacial layer with atomic level precision becomes critical to successful research on SrTiO₃.[1–3,8,19]

Among various interfacial properties listed above, the presence and roles of elemental vacancies become important to interpret the physical phenomena.[20,21] For example, the O vacancy (V_O) generated during pulsed laser deposition (PLD) growth is known as the source of increased conductivity.[22] The PLD process below oxygen pressure of 10^{-6} mbar can generate V_O on the substrate, which then converts SrTiO₃, a wide band gap ($\sim$3.2 eV) insulator, into a good conductor with a resistivity of <100 mΩ cm.[12,23] On the other hand, the creation of

[a] *Department of Physics and Photon Science, Gwangju Institute of Science and Technology, Gwangju 61005, Republic of Korea. E-mail: bsmun@gist.ac.kr*

[b] *Research Center for Materials Analysis, Korea Basic Science Institute, Daejeon 34133, Republic of Korea*

[c] *Beamline Research Division, Pohang Accelerator Laboratory, Pohang 37674, Republic of Korea. E-mail: kjkim@postech.ac.kr*

[d] *Center for Advanced X-ray Science, Gwangju Institute of Science and Technology, Gwangju 61005, Republic of Korea*

† Electronic supplementary information (ESI) available: Additional AP-XPS and AFM analyses. See DOI: 10.1039/d1tc03436g

‡ Equally contribute to this work.

Sr vacancies (V_{Sr}) is also known to occur under oxygen rich PLD conditions.[2,24,25] Under the presence of oxygen species on the SrTiO$_3$ surface, Sr atoms make surface migration to form SrO oxide at a cost of electrons in the subsurface region, *i.e.*, formation of an electron depletion layer near the surface.[2,24,26,27] In the case of V_{Sr} formation, the surface resistance increases, affecting the electrical properties of the interfacial layer. In fact, both types of V_O or V_{Sr} can occur simultaneously during the PLD process in which an oxygen environment and elevated temperature are required.[2,25] Thus, understanding the roles of these vacancies (V_O and V_{Sr}), so-called "defect chemistry", has become very important to achieve reliable functionality of SrTiO$_3$ heterostructure systems.

Previously, the creation and role of V_{Sr} were investigated by many research groups. Marchewka *et al.* observed the presence of a depletion layer at the Fe:SrTiO$_3$/Nb:SrTiO$_3$ interface associated with acceptor-type interface defects, V_{Sr}.[28] With the analysis of electron holography and numerical calculations, the creation of V_{Sr} and electron depletion layer were analyzed with changes in potential gradient at the interface. Also, with dynamic numerical simulations of high temperature MIT on n-type SrTiO$_3$, Meyer *et al.* explained the relationship between the surface charge region and V_{Sr}.[27] The simulation indicates that V_{Sr} plays an important role in connection of electrical conductivity of the n-SrTiO$_3$ substrate. In the meantime, the role of V_O has been also explored by many research groups. Kim *et al.* examined the correlation between structural phase transition (SPT) and V_O state in the SrRuO$_3$/SrTiO$_3$ system using *in situ* X-ray diffraction (XRD) and ambient pressure X-ray photoelectron spectroscopy (AP-XPS).[29] They demonstrated that the V_O formed at the SrRuO$_3$/SrTiO$_3$ interface determines the structural phase of the overlayer SrRuO$_3$ film. Moreover, with the application of isotope O^{18} on SrTiO$_3$, Lippert *et al.* identified the correlation between oxygen distribution and conductivity, indicating the critical roles of V_O at the LaAlO$_3$/SrTiO$_3$ interface.[30] Recently, with the aim of controlling V_O in SrTiO$_3$, Kang *et al.* demonstrated a new idea of growing an epitaxial thin film utilizing a SrTiO$_3$ substrate as an oxygen reservoir.[31] By controlling the oxygen content from the pre-substrate annealing process, the distribution of V_O concentration near the interfacial layer is optimized. That is, the SrTiO$_3$ substrate is utilized to provide a tunable oxygen environment for overlayer film growth. In particular, they pointed out the importance of the chemical environment during thin film fabrication, emphasizing the role of chemical state of substrate in generating accurate stoichiometry to the overlayer. Overall, the access to well-defined defect states on the SrTiO$_3$ substrate has become very important and critical to figure out the interfacial properties of complex oxide heterostructures based on SrTiO$_3$. On the other hand, Basletic *et al.*, from the spatial distribution of charge carriers on the LaAlO$_3$/SrTiO$_3$ interface layer with atomic force microscopy (AFM), showed that electron gas mobility is not affected by the degree of O vacancies, suggesting the alternate charge-transfer mechanism as a valid idea.[32]

In this report, to find out the role of the surface state of the substrate in the film growth process, *i.e.*, the role of defect states, we investigate the chemical/structural/electronic properties of an undoped SrTiO$_3$ (001) surface under film deposition conditions with application of AP-XPS and low energy electron diffraction (LEED). Previously, Andrä *et al.* utilized AP-XPS to investigate the chemical states of the electron depletion layer of the Nb-doped SrTiO$_3$ surface.[33,34] While their results show the evidence of the electron depletion layer due to the Sr segregation, the segregation of Sr is estimated by the presence of chemical shifts of XP spectra. In addition, Nb-doped SrTiO$_3$ is used to provide an electron reservoir for necessary access to XPS measurements.[35,36] However, it is previously reported that donor-doped SrTiO$_3$ can generate modified effective mass for conductivity, which can possibly affect the formation of the depletion layer.[37] In fact, it is a well-known fact that the doping process can make significant modification not only in the surface structure, but also in surface chemical/electronic properties. To avoid this uncertainty, an undoped SrTiO$_3$ substrate is employed for the study of O and Sr vacancies under ultrahigh vacuum (UHV, $< 10^{-9}$ mbar) to O$_2$ gas pressure of 0.1 mbar condition. In the comparison of chemical composition and surface structure under various atmospheric conditions, the sign of both O and Sr vacancies is clearly observed. While both vacancies produce almost identical surface chemical states with similar depth distribution, the density of states near the Fermi level (E_F) reveals the clear difference between the two vacancies, indicating different electronic states.

2. Experimental

Undoped SrTiO$_3$ (001) single crystalline films (10 $\times$ 10 $\times$ 0.5 mm^3, MaTeck GmbH) were grown by the flame fusion method. To achieve an atomically flat and TiO$_2$ terminated surface, an acid-etchant-free technique, combination of deionized (DI) water leaching and annealing process, was employed.[38] The film was annealed first at 1000 °C for 1 hour under atmospheric conditions and then rinsed with DI water for 30 sec at room temperature (RT) to dissolve the ionic bonded SrO layer.[38] After two cycles of the process, the topography of prepared SrTiO$_3$, using an AFM (XE-100, Park Systems), showed a step-terrace surface structure. (Fig. S1, ESI†) Later, an ordered surface of simple cubic (001) structure of SrTiO$_3$ surface was verified with LEED measurements (ErLEED 150, Specs GmbH).

Synchrotron-based AP-XPS measurements were carried out at PLS-II (8A2 beamline), Korea. The AP-XPS system consisting of the differentially pumped electrostatic lens and electron analyzer (PHOIBOS NAP 150, SPECS) allows the measurement of XP spectra up to a gas pressure of 25 mbar.[39] To characterize the surface chemical states of the SrTiO$_3$ (001) film at elevated temperature, *in situ* measurements were conducted during the thermal annealing process, up to 600 °C under both UHV and O$_2$ gas pressure of 0.1 mbar conditions, which generated surface V_O or V_{Sr}. An IR laser (dst11, OSTECH) was used for the annealing process.

All characteristic core level spectra of SrTiO$_3$ (O 1s, Ti 2p, and Sr 3d) were measured. In order to obtain depth profile
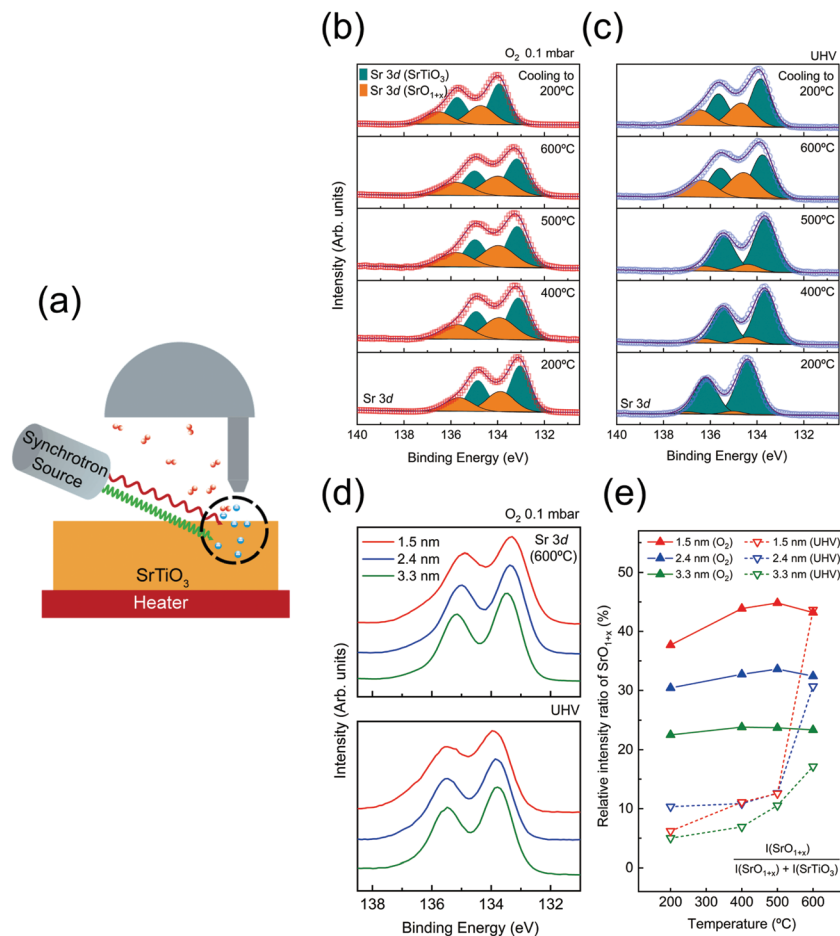
This journal is © The Royal Society of Chemistry 2021

J. Mater. Chem. C, 2021, **9**, 13094–13102 | **13095**

Fig. 1 (a) Experimental scheme of the depth-resolved AP-XPS measurement for identifying the surface redox chemistry of SrTiO$_3$ (001). (b and c) Sr 3d spectra, SrO$_{1+x}$ surface oxide (orange) and SrTiO$_3$ lattice oxide (cyan), measured under O$_2$ gas pressure of 0.1 mbar and UHV conditions as a function of annealing temperature. (d) The comparison of Sr 3d spectra at different probing depths under the conditions of O$_2$ 0.1 mbar (top) and UHV (bottom) at 600 °C. (e) Relative intensity ratio of the SrO$_{1+x}$ component, (SrO$_{1+x}$ component area/total Sr 3d spectral area) for each probing depth under both conditions as a function of annealing temperature.

information, *i.e.*, distribution of the surface space charge layer, depth-resolved AP-XPS measurements with variable X-ray photon energies were performed for 3 inelastic mean-free paths (IMFPs, λ = 0.5, 0.8, and 1.1 nm). For each probing depth (3λ), 1.5, 2.4, and 3.3 nm, the formula of Tanuma, Powell, and Penn (TPP) 2M was used to define the photon energies.[40] The photon energies used for each probing depth measurement are specified in Table S1 (ESI†). An experimental scheme of depth-resolved AP-XPS is displayed in Fig. 1(a).

It is to be noted that the X-ray-irradiated undoped SrTiO$_3$ sample experiences the space-charge effect due to the electrically insulating characteristics of SrTiO$_3$ near RT. In Table S2 (ESI†), the conductivity values of SrTiO$_3$ at our experimental temperature are estimated based on previous literature values and conductivity formula, $\sigma = CT^{-3/2}\exp(-E_g/2k_BT)$,[41–43] where C is a temperature-independent constant, T is the temperature, E_g is the band gap, and k_B is a Boltzmann constant. In conventional XPS measurements, the space charge effect starts to occur when conductivity becomes less than 10^{-10} Ω^{-1} m^{-1}.[44] According to Table S2

(ESI†), it is clear that the space charge effect is fully compensated when the temperature of the SrTiO$_3$ substrate reaches above 300 °C. Thus, all of our AP-XPS results above 300 °C are free from the charging problem. To analyze the XP spectra, the binding energy axis of all XP spectra was calibrated by the literature value of C 1s (284.5 eV) from intrinsic carbon species contained in the sample.[45] The position of the C 1s peak before the energy calibration can be checked in Table S3 (ESI†). However, as C species no longer exist above 500 °C under an oxygen environment, an Au foil attached to the sample was utilized for the XPS calibration purpose. That is, the binding energy peak of Au 4f$_{7/2}$ (84.0 eV) was used as a reference at 500 °C or above. In fact, under the condition in which charging is fully compensated while the carbon species remain on the surface, *i.e.*, sample temperatures between 300 °C and 500 °C, both C 1s and Au 4f$_{7/2}$ were utilized for calibration of binding energy, showing a consistent result with each other. The necessity and importance of careful assignment of binding energy to core levels can be further found in a previous report of Greczynski *et al.*[46]

3. Results and discussion

To begin with, AP-XPS measurements were performed during the annealing procedure, at 200, 400, 500, and 600 °C, and after cooling down (200 °C). All characteristic core level spectra under O_2 0.1 mbar (red) and UHV (blue) conditions at a probing depth of 1.5 nm are displayed in Fig. S2 (ESI†). If there is any charging effect due to photoirradiation, the binding energy position of XP spectra will be shifted to the higher binding energy direction with a distorted line shape. However, the XP spectra in Fig. S2 (ESI†) show no apparent sign of the charging effect. At 200 °C, the binding energy of O 1s and Sr 3d is slightly shifted to a higher binding direction, yet the line shape of the spectra is identical to the rest of the spectra at higher temperature. As explained in Table S2 (ESI†), the charging effect was sufficiently compensated when the SrTiO$_3$ film was annealed above 300 °C. Also, in Fig. S2(a–f) (ESI†), there are a couple of spectral dissimilarities between O_2 pressure and UHV conditions. One is the difference in binding energy position between oxygen and UHV conditions, *i.e.*, binding energy offset. The origin of the offset in binding energy will be discussed later. The other is the change of spectral line shape, particularly in Sr 3d spectra. When the temperature reaches 600 °C under UHV, the spectral weight of Sr 3d spectra at the higher binding energy side is significantly enhanced. In the case of annealing under O_2 pressure, the broadening of Sr 3d spectra started to appear even at 200 °C. This feature in Sr 3d spectra will be also examined further later with discussion on the formation of V_O and V_{Sr}.

In order to characterize the variation of chemical composition during annealing, Sr 3d spectra are analyzed in Fig. 1(b and c). Each Sr 3d spectrum is obtained at a surface sensitive depth of 1.5 nm, under O_2 pressure of 0.1 mbar [Fig. 1(b)] and UHV conditions [Fig. 1(c)]. The as-acquired spectra are plotted as red (blue) hollow symbols for the oxygen (UHV) environment. All spectra are de-convoluted with two doublets originating from SrTiO$_3$ and SrO$_{1+x}$ components, respectively. The SrTiO$_3$ component (cyan) indicates Sr bonding in the SrTiO$_3$ lattice while the SrO$_{1+x}$ component (orange) indicates Sr oxide on the topmost surface.[33,47,48] For the spectral fitting procedure, two Voigt doublets with a fixed branching ratio and spin orbit splitting are applied after the Shirley background is subtracted. The detailed fitting parameters are shown in Table S4 (ESI†).

In the case of the oxygen annealing process in Fig. 1(b), the presence of SrO$_{1+x}$ and SrTiO$_3$ components can be found in all temperature regions. As 0.1 mbar of O_2 gas is introduced, the surface oxide is formed on the SrTiO$_3$ film surface even at a temperature as low as 200 °C. In contrast, under UHV conditions, the sign of SrO$_{1+x}$ surface oxide is very minimal at 200 °C, as shown in Fig. 1(c). This comparison of Sr 3d spectra between oxygen pressure and UHV implies that the formation of the SrO$_{1+x}$ component is not coming from air exposure of the sample. Rather, it indicates that introduced O_2 gas molecules are dissociated and bound to Sr on the surface even at 200 °C. Fig. 1(b) shows that the SrO$_{1+x}$ surface oxide formed under

oxygen pressure remains constant without much changes until 600 °C. In the case of UHV conditions, the formation of surface oxide starts to appear only at 600 °C, as shown in Fig. 1(c). Under both conditions, the surface oxide remains on the surface after the temperature is cooled down to 200 °C.

To compare the chemical states of Sr oxide with varied probing depth under oxygen and UHV environments, Sr 3d spectra (600 °C) at a probing depth of 1.5 (red), 2.4 (blue), and 3.3 nm (green), are plotted in Fig. 1(d). It clearly shows that both figures of Fig. 1(d) show the higher intensity of SrO$_{1+x}$ in the 1.5 nm region, indicating that the formation of surface oxide occurs at the surface. Furthermore, in order to have a quantitative comparison of SrO$_{1+x}$ surface oxide evolution, the relative intensity ratio of the SrO$_{1+x}$ component is plotted together as a function of annealing temperature, as shown in Fig. 1(e). The relative intensity ratio of the SrO$_{1+x}$ component [SrO$_{1+x}$ component area/total Sr 3d spectral area] is plotted on each fitted Sr 3d spectrum. Again, it is to be noted that chemical compositions are clearly different at the first annealing temperature step, 200 °C, between two different atmosphere conditions. In the 1.5 nm region, the relative intensity value of SrO$_{1+x}$ is ∼38% under oxygen conditions while that of UHV is only ∼6%. Under an O_2 environment, the relative intensity ratio of SrO$_{1+x}$ remains similar throughout the entire temperature range, *i.e.*, no sign of subsurface evolution to surface SrO$_{1+x}$ oxide. A closer look at Fig. 1(e) shows that the surface oxides in the 1.5 nm region continue to increase while the oxide components at 2.4 nm and 3.3 nm remain almost constant, revealing the sign of impeding oxygen diffusion. On the other hand, the intensity ratio of SrO$_{1+x}$ under UHV conditions shows no significant changes until the temperature reaches 600 °C. Under UHV conditions, a rapid increase of SrO$_{1+x}$ surface oxide from 6% (at 200 °C) to 45% (at 600 °C) was observed at 1.5 nm probing depth. An interesting point is that the relative intensity ratio of SrO$_{1+x}$ oxide of UHV conditions matches well with that of O_2 environment conditions at 600 °C. In quantitative comparison of the SrO$_{1+x}$ spectra of O_2 and UHV environments at 600 °C, relative amounts of SrO$_{1+x}$ are almost the same at a probing depth of 1.5 nm, *i.e.*, ∼43%. While the other two probing depths show a slight difference, the difference is clearly reduced. To illustrate this point, Sr 3d spectra at a probing depth of 1.5 nm ($T = 600$ °C) from two conditions are plotted together in Fig. S3 (ESI†). Fig. S3 (ESI†) shows that the surface oxides formed under two different conditions, UHV and oxygen pressure, are having almost identical chemical states.

While the chemical states of the surface SrO$_{1+x}$ layer in Fig. S3 (ESI†) are similar, the formation process of oxides is very different. In the case of the oxygen annealing step, it can be interpreted that the stable SrO$_{1+x}$ passive layer is formed at topmost surface from the interaction of externally provided dissociated oxygen atoms with the surface migrated Sr atom from bulk, which in turn inhibits oxygen diffusion into the bulk side.[27,49] On the other hand, the UHV annealing process, reducing condition for most of the metal oxide system, is expected to create oxygen defect states, as reported in many

This journal is © The Royal Society of Chemistry 2021

J. Mater. Chem. C, 2021, **9**, 13094–13102 | **13097**

previous SrTiO₃ studies.[2,22,25] Until the temperature below 500 °C, no significant change in Sr 3d spectra is found across all depth ranges. However, when the temperature reaches 600 °C under UHV, a chemically stable SrO_{1+x} surface oxide is formed on the topmost surface as shown in Sr 3d spectra in Fig. 1(c). The origin of the SrO_{1+x} surface oxide will be provided later with the discussion of LEED. The V_O feature can be also identified in Ti 2p and valence band (VB) spectra. The gray shaded area in Fig. S4(d) and S5 (ESI†) clearly reveals the enhancement of spectral weight as temperature increases, corresponding to emergence of Ti^{3+} component and formation of V_O during the UHV annealing process. Overall, during the UHV annealing process, the TiO₂ layer in SrTiO₃ is gradually reduced and V_O is left behind.[50,51]

Next, in order to identify any changes in surface structural ordering after surface chemical rearrangement by the previous annealing procedure under both oxygen and UHV conditions, the measurements of LEED are carried out immediately after the AP-XPS measurements without the exposure to air, *i.e.*, the measurement of *in situ* LEED. Fig. 2(a) displays the LEED patterns of the as-prepared, oxygen annealed, and UHV annealed SrTiO₃ (001) surface. The annealing temperature is 600 °C. The characteristics of the (001) oriented cubic structure are explicitly identified in all patterns. Compared with the LEED pattern of the "as-prepared" SrTiO₃ (001) surface, in principle both LEED patterns of "after O₂ annealing" and "after UHV annealing" reveal the superstructure pattern, although the superstructure pattern is slightly blurred for the "after UHV annealing" image. For accurate structural analysis, all systematic distortions in LEED images in Fig. 2(a) are corrected and the patterns are simulated by the numerical fitting procedure as displayed in Fig. 2(b).[52] Then, the lattice structures in real space are illustrated in Fig. 2(c) *via* inverse Fourier transform of

Fig. 2(b). The yellow circles represent the basic lattice structure of SrTiO₃ (001), and the purple circles represent the lattice structure of the reconstructed topmost surface from annealing. The unit cell is defined as a red square in Fig. 2(c).

As discussed before, SrO_{1+x} surface oxide is formed on the SrTiO₃ topmost surface during both O₂ and UHV annealing at 600 °C. In the LEED pattern of "after O₂ annealing", there exist sub-patterns shown as low intensity spots between the strong (001) spots. The presence of new superstructure patterns shows that stable SrO_{1+x} clusters form an ordered c(6 × 2) surface structure on SrTiO₃ (001). Also, in the case of "after UHV annealing", an identical c(6 × 2) superstructure pattern is formed on SrTiO₃ (001). However, low intensity of the superstructure pattern in LEED indicates the presence of a less ordered surface structure during UHV annealing. In fact, it is well known that the concentration of surface defects increases under UHV annealing, which can blur the LEED image.

Previously, several numbers of surface reconstructions of SrTiO₃ (001) have been reported, such as (1 × 1), (2 × 1), (4 × 4), c(4 × 2), c(4 × 4), and $(\sqrt{13} \times \sqrt{13})$-R33.7°, including c(6 × 2).[53,54] Many studies using surface sensitive techniques such as AFM, scanning tunneling microscopy (STM), reflection high-energy electron diffraction (RHEED) and density functional theory (DFT) were carried out to figure out these various reconstructed phases.[55–60] Nevertheless, their conclusions are still unclear due to their instability and extreme sensitivity to thermodynamic conditions. In regard to the c(6 × 2) phase, the presence of c(6 × 2) reconstruction on SrTiO₃ (001) from UHV and oxygen annealing was observed with RHEED and LEED study.[60,61] Our Sr 3d LEED results clearly show the stable c(6 × 2) reconstruction taking place on the SrTiO₃ (001) surface by both O₂ (0.1 mbar) and UHV ($<10^{-9}$ mbar) annealing at 600 °C, *i.e.*, the formation of a nearly identical surface structure for both conditions. To our knowledge, no direct comparison of LEED patterns has been made between oxygen and UHV annealed SrTiO₃ (001) surfaces.

To look into the details of chemical states of surface oxide, the binding energy position of core level spectra of SrTiO₃ is carefully monitored. Fig. 3(a) exhibits the characteristic binding energy values of the SrTiO₃ lattice component during both oxygen and UHV thermal annealing processes. The probing depth of all spectra was 1.5 nm, providing the most surface sensitive information in our measurement. The binding energy positions of O 1s, Ti $2p_{3/2}$, and Sr $3d_{5/2}$ are plotted as black, red, and blue, respectively, and the solid (dotted) line indicates the binding energy positions under O₂ (UHV) annealing conditions. The binding energy positions of each spectrum can be found in Table S5 (ESI†). In Fig. 3(a), the binding energy offset of all elements between oxygen and UHV environments can be noticed, as discussed with Fig. S2 (ESI†). Except for the case of 200 °C where the possible charging issues could occur, the binding energy positions of all elements under oxygen atmosphere are lower than those under UHV by as much as ∼0.54 eV in all temperature ranges, shown under the gray shaded area in Fig. 3(a). The identified values of the offset are
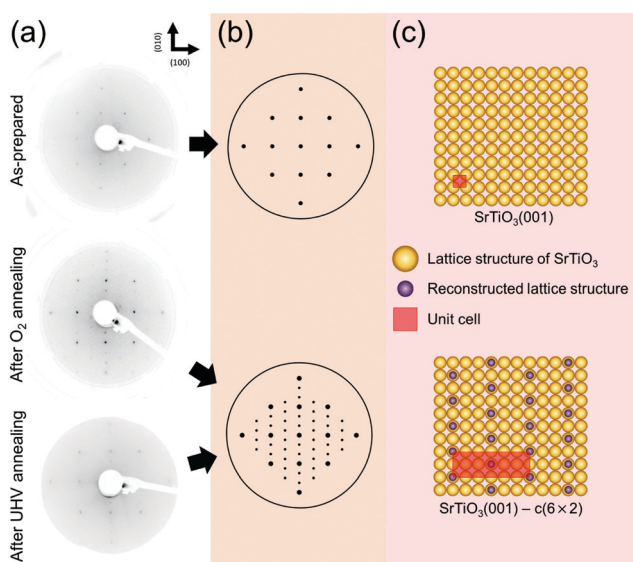

Fig. 2 (a) LEED patterns of the as-prepared, O₂ annealed and UHV annealed SrTiO₃ (001) surface at 600 °C. (b) Simulated LEED patterns for structural analysis. (c) The illustrations of lattice structures in real space.
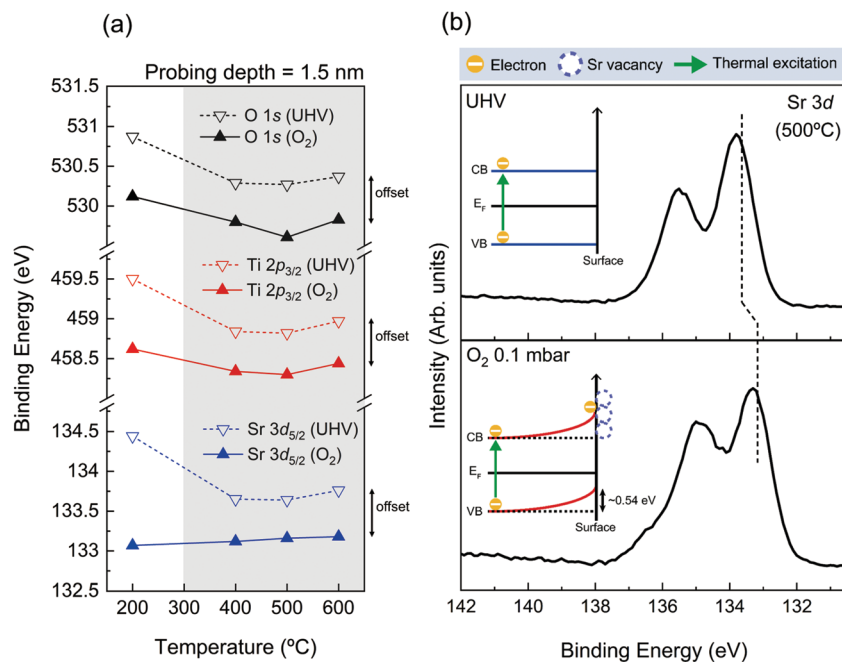
Fig. 3 (a) Characteristic binding energy positions of the SrTiO$_3$ lattice component as a function of annealing temperature. [Each core level O 1s, Ti 2p$_{3/2}$, and Sr 3d$_{5/2}$ is shown in black, red, and blue colors while the solid (dotted) line indicates the binding energy positions under O$_2$ 0.1 mbar (UHV) annealing conditions.] (b) Sr 3d spectra under UHV (up) and O$_2$ (down) environments at 500 °C for the probing depth of 1.5 nm taken from Fig. 1(c and b). The dotted vertical lines in (b) indicate the binding energy positions of the SrTiO$_3$ lattice component. The illustrations of band alignment under both annealing conditions are displayed in the inset of (b), respectively.

shown in Table S5 (ESI†). As one example of this offset, Sr 3d spectra measured at 500 °C under two different conditions are compared in Fig. 3(b). Fig. 3(b) clearly shows that there exists not only a difference in spectral shape due to the difference in chemical composition, but the offset of binding energy position under two atmospheric conditions.

In fact, the presence of the binding energy offset in the oxygen annealing process can be correlated with the formation of the space charge layer discussed in our introduction. According to the previous reports on space charge layer study on the Nb-doped SrTiO$_3$ surface, V_{Sr} is generated while consuming electrons on the surface during the O$_2$ annealing process,[33,34] generating 0.55–0.60 eV core level shift in AP-XPS measurements. While the amount of this core level shift is almost identical to what is observed in Fig. 3, the origin is different. In the case of the Nb-doped SrTiO$_3$ surface, the electron source for the surface charge layer, *i.e.* electron depletion layer, was provided from the substrate. Here, in the case of our undoped SrTiO$_3$ system, electrons can be provided sufficiently by thermal excitation at temperature above 300 °C. In the O$_2$ annealing process, thermally excited electrons are trapped by the V_{Sr} at the surface, which forms an electron depletion layer near the surface. Moreover, the mismatch of electron density between the surface electron depletion layer and bulk can create the VB bending near the Fermi level. The schematic of upward band bending during O$_2$ annealing is illustrated in the inset of Fig. 3(b) in the rigid band model. Furthermore, this band bending phenomenon is identified by VB analysis in Fig. S6

(ESI†). The positions of the valence band maximum (VBM) under O$_2$ conditions as a function of annealing temperature are displayed in Fig. S6 (ESI†). As annealing temperature increases from 200 °C up to 600 °C, the position of the VBM is gradually shifted up to ~0.38 eV. Since a sufficient electron depletion layer has not yet formed due to less thermal electrons at 200 °C, the VB hardly moves. Then, the position of the VBM is shifted to a lower binding energy direction as temperature increases, indicating the onset of the surface space charge layer. At higher annealing temperature, the upward band bending becomes more pronounced. In the meantime, the important thing to be checked before the characterization of the space charge layer is the scale of Debye length. As can be found in Table S6 (ESI†), the length scale of the space charge layer is much smaller than Debye length in our condition, demonstrating that the above discussions on the nature of the space charge layer are valid.

On the other hand, the electron depletion and band bending could also occur under UHV conditions as our AP-XPS and LEED results confirm the formation of the SrO$_{1+x}$ surface under the UHV annealing process. However, as described before, when the temperature reaches 600 °C under UHV conditions, the TiO$_2$ layer starts to get reduced and V_O is formed as shown in Fig. S4(d) and S5 (ESI†). In this case, extra sources of electrons are generated, limiting the formation of the electron depletion layer and band bending at the surface. Overall, the presence of binding energy offset in Fig. 3 indicates that completely different surface electronic structures are formed in each annealing process. Up to now, we have shown that the
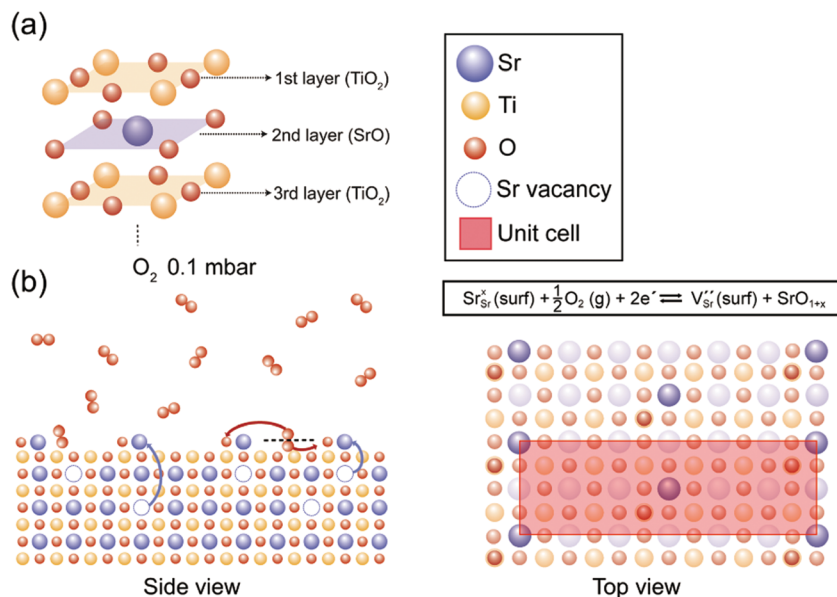
This journal is © The Royal Society of Chemistry 2021

J. Mater. Chem. C, 2021, **9**, 13094–13102 | **13099**

Fig. 4 (a) The schematic illustration of the layer structure from the top surface of the as-prepared $SrTiO_3$ (001). (b) The proposed surface redox process in side and top views during the annealing under O_2 0.1 mbar. [Sr, Ti, and O atoms are indicated as blue, yellow and red circles, respectively, and each vacancy is expressed as a dotted circle of the corresponding color.] Top view displays the formation of SrO_{1+x} with a $c(6 \times 2)$ superstructure confirmed by LEED analysis in Fig. 2(c). The surface redox reaction formula describes the formation of V_{Sr} and SrO_{1+x} while consuming electrons under O_2 annealing conditions.

chemical states and structures of surface SrO_{1+x} oxide are very much similar in both UHV and oxygen annealing processes. Yet, the results of Fig. 3 clearly show that the difference of the electronic structures is an important parameter that can define the characteristics of surface defect states of $SrTiO_3$ (001).

In Fig. 4, our understanding of surface reconstruction on $SrTiO_3$ (001) during oxygen annealing is illustrated. Initially, O_2 gas molecules (red circles) are dissociated on the $SrTiO_3$ surface under oxygen atmosphere conditions. As the temperature increases, Sr atoms underneath the surface are pulled over to the outermost layer by external oxygen (Fig. 4(b) side view) and SrO_{1+x} clusters are formed on the surface with $c(6 \times 2)$ surface ordering as shown in Fig. 4(b) top view. The surface chemical redox reaction is described at the top of Fig. 4(b) top view using Kröger–Vink notations. It should be noted that V_{Sr} is formed with SrO_{1+x} surface oxide on the surface while consuming electrons under an oxygen atmosphere, implying the formation of a space charge layer. On the other hand, during UHV annealing, there is considerable SrO_{1+x} formation only when the temperature reaches 600 °C. Again, during UHV annealing, SrO_{1+x} surface oxide is formed on the topmost surface with a $c(6 \times 2)$ reconstruction phase, as explained through the LEED analysis in Fig. 2. Although a few models have been suggested, which focus on the formation of vacancies and their role in atomic rearrangement between Sr and O atoms during the annealing process, the exact understanding on the origin of surface reconstruction for $SrTiO_3$ (001) under UHV conditions is still in debate.[53,57,59–61] Our result from the UHV annealing process suggests that the surface reconstruction occurs as V_O and Ti vacancies (V_{Ti}) interact with Sr atoms at the top surface,

resulting in chemically stable SrO_{1+x} surface oxide with a $c(6 \times 2)$ surface restructure.

Finally, we would like to make comments on the doped-$SrTiO_3$ system. Compared to the previous result of the Nb-doped $SrTiO_3$ surface,[43] our results on the undoped $SrTiO_3$ surface show similar degrees of band bending effect, ~ 0.54 eV, showing that the degree of the charge depletion layer is similar. However, in the case of Nb-doped $SrTiO_3$, the previous group obtained the degree of band bending from the comparison of core level spectra of different probing depths. In our case of undoped $SrTiO_3$, the degree of band bending is obtained from direct comparison between UHV and oxygen annealing conditions, which provides absolute pressure-dependent feature in AP-XPS. In addition, the core level positions of the Sr 3d peak of Nb-doped $SrTiO_3$ show a gradual shift to a higher binding energy side as the probing depth increases while our undoped $SrTiO_3$ surface shows almost constant binding energy in the entire spectra [Fig. 1], displaying a clear difference of chemical states from the surface to bulk layer.

4. Conclusions

With depth resolved AP-XPS and LEED analysis, we compared the chemical/structural/electronic states of the undoped $SrTiO_3$ (001) surface under UHV and O_2 pressure of 0.1 mbar conditions to identify the role of the surface state of the substrate. Our observations reveal that, under an oxygen environment, Sr elements are being pulled over to the outermost layer and chemically stable surface oxide, SrO_{1+x} with a $c(6 \times 2)$ super-structure, is formed while forming an electron depletion layer

underneath the surface. Furthermore, the modification of the electronic structure due to the electron depletion layer is confirmed as band bending near the Fermi level starts to appear. On the other hand, under UHV annealing conditions, the vacancy-related SrO_{1+x} surface oxide formed at ~ 600 °C. The SrO_{1+x} surface oxide is chemically and structurally identical to those in the oxygen environment, yet the origin of oxide formation is different. Our findings suggest that the surface electronic structure of the substrate has a greater influence on the properties of complex oxide heterostructures than other parameters. This work provides a deeper understanding on the surface charge layer of undoped $SrTiO_3$ (001), which can be useful for study of the $SrTiO_3$-based complex oxide heterostructure.

Author contributions

Hojoon Lim and Chanyang Song: conceptualization, experiment, data acquisition, formal analysis, and writing – original draft & editing. Minsik Seo, Dongwoo Kim, Moonjung Jung, Habin Kang, Seunghwan Kim, Kyung-Jae Lee, Youngseok Yu, and Geonhwa Kim: experiment and formal analysis. Ki-jeong Kim and Bongjin Simon Mun: supervision, writing – review & editing, formal analysis, funding acquisition, and project administration.

Conflicts of interest

There are no conflicts to declare.

Acknowledgements

References

1 Y. Tokura, M. Kawasaki and N. Nagaosa, *Nat. Phys.*, 2017, **13**, 1056–1068.

2 J. Zhu, J. W. Lee, H. Lee, L. Xie, X. Pan, R. A. De Souza, C. B. Eom and S. S. Nonnenmann, *Sci. Adv.*, 2019, **5**, 1–10.

3 P. Zubko, S. Gariglio, M. Gabay, P. Ghosez and J. M. Triscone, *Annu. Rev. Condens. Matter Phys.*, 2011, **2**, 141–165.

4 C. H. Ahn, K. M. Rabe and J. M. Triscone, *Science*, 2004, **303**, 488–491.

5 A. Brinkman, M. Huijben, M. Van Zalk, J. Huijben, U. Zeitler, J. C. Maan, W. G. Van Der Wiel, G. Rijnders, D. H. A. Blank and H. Hilgenkamp, *Nat. Mater.*, 2007, **6**, 493–496.

6 A. Gozar, G. Logvenov, L. F. Kourkoutis, A. T. Bollinger, L. A. Giannuzzi, D. A. Muller and I. Bozovic, *Nature*, 2008, **455**, 782–785.

7 A. Ohtomo and H. Y. Hwang, *Nature*, 2004, **427**, 423–426.

8 D. K. Bediako, M. Rezaee, H. Yoo, D. T. Larson, S. Y. F. Zhao, T. Taniguchi, K. Watanabe, T. L. Brower-Thomas, E. Kaxiras and P. Kim, *Nature*, 2018, **558**, 425–429.

9 T. Kim, S. Fan, S. Lee, M.-K. Joo and Y. H. Lee, *Sci. Rep.*, 2020, **10**, 1–8.

10 Y.-Y. Lu, C.-R. Guo, H.-L. Yeh, H.-W. Chen, C.-C. Kuo, J.-H. Hsu, J. Jhou, Y.-T. Huang, S.-H. Hsieh, C.-H. Chen, C.-H. Ho, R. Sankar and F.-C. Chou, *ACS Appl. Nano Mater.*, 2020, **3**, 11769–11776.

11 E. Pomerantseva and Y. Gogotsi, *Nat. Energy*, 2017, **2**, 1–6.

12 Y. Y. Pai, A. Tylan-Tyler, P. Irvin and J. Levy, *Rep. Prog. Phys.*, 2018, **81**, 036503.

13 O. F. Shoron, S. Raghavan, C. R. Freeze and S. Stemmer, *Appl. Phys. Lett.*, 2017, **110**, 232902.

14 A. Verma, S. Raghavan, S. Stemmer and D. Jena, *Appl. Phys. Lett.*, 2015, **107**, 2–6.

15 C. S. Koonce, M. L. Cohen, J. F. Schooley, W. R. Hosler and E. R. Pfeiffer, *Phys. Rev.*, 1967, **163**, 380.

16 J. Garcia-Barriocanal, A. Rivera-Calzada, M. Varela, Z. Sefrioui, E. Iborra, C. Leon, S. J. Pennycook and J. Santamaria, *Science*, 2008, **321**, 676–680.

17 D. Di Castro, C. Cantoni, F. Ridolfi, C. Aruta, A. Tebano, N. Yang and G. Balestrino, *Phys. Rev. Lett.*, 2015, **115**, 1–5.

18 N. Nakagawa, H. Y. Hwang and D. A. Muller, *Nat. Mater.*, 2006, **5**, 204–209.

19 K. L. Tai, C. W. Huang, R. F. Cai, G. M. Huang, Y. T. Tseng, J. Chen and W. W. Wu, *Small*, 2020, **16**, 1–10.

20 C. Xie, D. Yan, H. Li, S. Du, W. Chen, Y. Wang, Y. Zou, R. Chen and S. Wang, *ACS Catal.*, 2020, **10**, 11082–11098.

21 J. Maier, *Angew. Chem., Int. Ed. Engl.*, 1993, **32**, 313–335.

22 F. Gunkel, D. V. Christensen, Y. Z. Chen and N. Pryds, *Appl. Phys. Lett.*, 2020, **116**, 120505.

23 S. A. Lee, H. Jeong, S. Woo, J. Y. Hwang, S. Y. Choi, S. D. Kim, M. Choi, S. Roh, H. Yu, J. Hwang, S. W. Kim and W. S. Choi, *Sci. Rep.*, 2016, **6**, 1–10.

24 M.-A. Rose, B. Šmid, M. Vorokhta, I. Slipukhina, M. Andrä, H. Bluhm, T. Duchoň, M. Ležaić, S. A. Chambers, R. Dittmann, D. N. Mueller and F. Gunkel, *Adv. Mater.*, 2021, **33**, 2004132.

25 P. P. Balakrishnan, M. J. Veit, U. S. Alaan, M. T. Gray and Y. Suzuki, *APL Mater.*, 2019, **7**, 011102.

26 R. Meyer, R. Waser, J. Helmbold and G. Borchardt, *Phys. Rev. Lett.*, 2003, **90**, 105901.

27 R. Meyer, A. F. Zurhelle, R. A. De Souza, R. Waser and F. Gunkel, *Phys. Rev. B*, 2016, **94**, 1–19.

28 A. Marchewka, D. Cooper, C. Lenser, S. Menzel, H. Du, R. Dittmann, R. E. Dunin-Borkowski and R. Waser, *Sci. Rep.*, 2014, **4**, 1–6.

29 D. Kim, H. Lim, S. S. Ha, O. Seo, S. S. Lee, J. Kim, K. Kim, L. Perez Ramirez, J.-J. Gallet and F. Bournel, et al., *J. Chem. Phys.*, 2020, **152**, 34704.

30 C. W. Schneider, M. Esposito, I. Marozau, K. Conder, M. Doebeli, Y. Hu, M. Mallepell, A. Wokaun and T. Lippert, *Appl. Phys. Lett.*, 2010, **97**, 2008–2011.

This journal is © The Royal Society of Chemistry 2021

J. Mater. Chem. C, 2021, **9**, 13094–13102 | **13101**

31 K. T. Kang, B. Zhang, Y. Sharma, B. Paudel, H. Wang, P. Dowden and A. Chen, *Appl. Phys. Lett.*, 2020, **117**, 151601.

32 M. Basletic, J.-L. Maurice, C. Carrétéro, G. Herranz, O. Copie, M. Bibes, É. Jacquet, K. Bouzehouane, S. Fusil and A. Barthélémy, *Nat. Mater.*, 2008, **7**, 621–625.

33 M. Andrä, H. Bluhm, R. Dittmann, C. M. Schneider, R. Waser, D. N. Mueller and F. Gunkel, *Phys. Rev. Mater.*, 2019, **3**, 1–9.

34 M. Andrä, F. Dvořák, M. Vorokhta, S. Nemšák, V. Matolín, C. M. Schneider, R. Dittmann, F. Gunkel, D. N. Mueller and R. Waser, *APL Mater.*, 2017, **5**, 56106.

35 A. Spinelli, M. A. Torija, C. Liu, C. Jan and C. Leighton, *Phys. Rev. B: Condens. Matter Mater. Phys.*, 2010, **81**, 1–14.

36 C. Rodenbücher, M. Luysberg, A. Schwedt, V. Havel, F. Gunkel, J. Mayer and R. Waser, *Sci. Rep.*, 2016, **6**, 1–8.

37 W. Wunderlich, H. Ohta and K. Koumoto, *Phys. B*, 2009, **404**, 2202–2212.

38 J. G. Connell, B. J. Isaac, G. B. Ekanayake, D. R. Strachan and S. S. A. Seo, *Appl. Phys. Lett.*, 2012, **101**, 98–101.

39 G. Kim, Y. Yu, H. Lim, B. Jeong, J. Lee, J. Baik, B. S. Mun and K. Kim, *J. Synchrotron Radiat.*, 2020, **27**, 507–514.

40 S. Tanuma, C. J. Powell and D. R. Penn, *Surf. Interface Anal.*, 1994, **21**, 165–176.

41 N. G. Eror and U. Balachandran, *J. Solid State Chem.*, 1982, **42**, 227–241.

42 T. Bieger, J. Maier and R. Waser, *Solid State Ionics*, 1992, **53–56**, 578–582.

43 W. D. Callister Jr. and D. G. Rethwisch, *Materials Science and Engineering – An Introduction 10th Edition*, 2018.

44 W. D. Callister Jr., D. G. Rethwisch, J. V. Sci, K. Artyushkova, H. Cohen, C. D. Easton, D. J. Morgan, M. Engelhard, T. R. Gengenbach, G. Greczynski, P. Mack and D. J. Morgan, *J. Vac. Sci. Technol., A*, 2020, **38**, 031204.

45 J. F. Moulder, W. F. Stickle, P. E. Sobol and K. D. Bomben, *Handbook of X-ray Photoelectron Spectroscopy*, United States of America, 1993.

46 G. Greczynski and L. Hultman, *Sci. Rep.*, 2021, **11**, 1–5.

47 R. C. Hatch, M. Choi, A. B. Posadas and A. A. Demkov, *J. Vac. Sci. Technol., B: Nanotechnol. Microelectron.: Mater., Process., Meas., Phenom.*, 2015, **33**, 061204.

48 G. M. Vanacore, L. F. Zagonel and N. Barrett, *Surf. Sci.*, 2010, **604**, 1674–1683.

49 R. A. De Souza, V. Metlenko, D. Park and T. E. Weirich, *Phys. Rev. B: Condens. Matter Mater. Phys.*, 2012, **85**, 1–11.

50 T. Nishimura, A. Ikeda, H. Namba, T. Morishita and Y. Kido, *Surf. Sci.*, 1999, **421**, 273–278.

51 A. R. Silva and G. M. Dalpian, *J. Appl. Phys.*, 2014, **115**, 33710.

52 F. Sojka, M. Meissner, C. Zwick, R. Forker and T. Fritz, *Rev. Sci. Instrum.*, 2013, **84**, 015111.

53 T. Kubo and H. Nozoye, *Surf. Sci.*, 2003, **542**, 177–191.

54 Y. Lin, A. E. Becerra-toledo, F. Silly, K. R. Poeppelmeier, M. R. Castell and L. D. Marks, *Surf. Sci.*, 2011, **605**, L51–L55.

55 Z. Wang, F. Li, S. Meng, J. Zhang, E. W. Plummer, U. Diebold and J. Guo, *Phys. Rev. Lett.*, 2013, **111**, 1–5.

56 T. Kubo, H. Orita and H. Nozoye, *Phys. Chem. Chem. Phys.*, 2011, **13**, 16516–16519.

57 C. H. Lanier, A. Van De Walle, N. Erdman, E. Landree, O. Warschkow, A. Kazimirov, K. R. Poeppelmeier, J. Zegenhagen, M. Asta and L. D. Marks, *Phys. Rev. B: Condens. Matter Mater. Phys.*, 2007, **76**, 1–9.

58 N. Erdman, O. Warschkow, M. Asta, K. R. Poeppelmeier, D. E. Ellis and L. D. Marks, *J. Am. Chem. Soc.*, 2003, **125**, 10050–10056.

59 M. R. Castell, *Surf. Sci.*, 2002, **505**, 1–13.

60 M. Naito and H. Sato, *Phys. C*, 1994, **229**, 1–11.

61 Q. D. Jiang and J. Zegenhagen, *Surf. Sci.*, 1999, **425**, 343–354.

13102 | *J. Mater. Chem. C*, 2021, **9**, 13094–13102

This journal is © The Royal Society of Chemistry 2021